B.Y. Zhou, N.R. Gauger, M. Morelli, A. Guardone, J. Hauth, X. Huan
Development of a Real-Time In-Flight Ice Detection System via Computational Aeroacoustics and Bayesian Neural Networks
In: AIAA Scitech 2020 Forum, Orlando, FL, USA, 6-10 Jan. 2020, ISBN: 978-1-62410-595-1, Paper AIAA 2020-1638, doi:10.2514/6.2020-1638

Development of a Real-Time In-Flight Ice Detection System via Computational Aeroacoustics and Bayesian Neural Networks

Beckett Y. Zhou* and Nicolas R. Gauger†
Chair for Scientific Computing, TU Kaiserslautern
Bldg 34, Paul-Ehrlich-Strasse, 67663 Kaiserslautern, Germany

Myles Morelli‡ and Alberto Guardone§
Department of Aerospace Sciences and Technologies, Politecnico di Milano
Building B12 Campus Bovisa, Via La Masa, 34 20156 Milano, Italy

Jeremiah Hauth¶ and Xun Huan‖
Department of Mechanical Engineering, University of Michigan
1231 Beal Ave, Ann Arbor, MI 48109-2133, USA

Reliable real-time detection of ice formation is a critical enabling technology in improving rotorcraft safety. The development of a real-time in-flight ice detection system using computational aeroacoustics and Bayesian neural networks is presented and evaluated within this paper. A finite NACA0012 airfoil section undergoing sinusoidal pitching is used to represent the cyclic motion characteristic of a rotor in forward flight. Experimental ice shape measurements from the NASA Glenn Icing Research Wind Tunnel are used for validation of the numerical ice shapes. The flow-fields of the computed ice shapes are then determined using a hybrid RANS/LES approach and the acoustic noise signals of the ice shapes are predicted using the solid-surface Ffowcs Williams and Hawkings (FWH) analogy. A Bayesian neural network is then trained using the ice shapes and the performance indicators are mapped to the acoustic noise signals. This framework thus allows for the detection of ice and significantly the type of ice accreted over the pitching wing through differentiating between iced noise signals.

I. Introduction

In-flight icing is widely recognized as a significant hazard to flight safety due to the negative impact it induces on aircraft performance and handling qualities.[1] Unlike fixed-wing aircraft, rotorcraft are unable to escape icing conditions via climbing to high enough altitudes where the presence of super-cooled water droplets decreases. In conjunction, in situ observations from reconnaissance aircraft has shown that it is in precisely the flight envelope in which rotorcraft typically operate where super-cooled water droplets naturally thrive to exist.[2] In the US alone since as lately as 2016, there have been multiple in-flight rotorcraft icing accidents recorded, many of which involved fatalities.[3–5] A widespread consensus and coherent understanding on the most appropriate methods for mitigating in-flight icing however remains far from being satisfactory.

The ice accretion process can be distinguished as either rime, glaze or mixed ice and is primarily dependent upon the outside air temperature. Rime ice dominates during the coldest conditions. Rime ice accretes when supercooled water droplets instantaneously freeze when impacting on a sub-zero surface and can be characterized by an opaque appearance due to air bubbles being trapped during the phase changing process. A rime ice profile may take the form

*Research Scientist, Member AIAA, yuxiang.zhou@scicomp.uni-kl.de
†Professor, Associate Fellow AIAA, nicolas.gauger@scicomp.uni-kl.de
‡PhD Candidate, Member AIAA, mylescarlo.morelli@polimi.it
§Professor, alberto.guardone@polimi.it
¶PhD Candidate, Student Member AIAA, hauthj@umich.edu
‖Assistant Professor, Member AIAA, xhuan@umich.edu

of a pointed *spearhead* if the rate of ice accretion is high. Glaze ice dominates during much higher conditions closer to the melting temperature of ice. Glaze ice accretes when supercooled water droplets impact on the surface and run-back before freezing. This allows the air bubbles to escape before freezing so gives rise to a transparent ice structure. A glaze ice profile may take the form of *double-horns*. Establishing which type of ice profile is forming is hence important to understand the negative performance metrics which are associated with the ice structure.

Aircraft anti-icing and de-icing methods can be categorized into three main groups, including freezing point depressants, thermal melting systems and surface deformations.[6] Recently, anti-icing and de-icing systems have undergone significant development,[7–9] however despite this, current anti-icing and de-icing systems are not without their issues and drawbacks. One of the main drawbacks of ice protection systems is that very few are suitable for rotorcraft. Moreover, rotorcraft have limited power available and ice protection systems that are suitable tend to have a high power consumption meaning that very few are actually installed. While searching to improve the safety and performance of aircraft in hostile environments, methods and techniques for detecting and characterizing ice structures during flight have become highly desirable to potentially increase the efficiency and optimize anti- and de-icing systems.

Acknowledging this, ice detection and monitoring systems have been developed and can be grouped into direct and indirect measurement approaches. The indirect approach for detecting ice formation is based on the relationship between the ice accretion and negative performance metrics which it has on the aircraft, such as the lift and drag.[10] While the direct approach for detecting ice formation uses surface measurement techniques to assess changes in the properties of the iced surface.[11] The direct approach has been seen to be preferable as by the time ice has influenced the aircraft's performance it is often too late. One of the main issues with many of the direct approaches however is that their implementation on aircraft is challenging. This concern can be expressed for instance on rotorcraft where the use of small sensors on moving components such as rotor blades would be highly unpractical.

To address this issue, this work looks to help develop an indirect ice detection method capable of being implemented on complex aircraft configurations such as rotorcraft to help improve flight safety. This work seeks to build upon previous experimental studies intuition of using noise for monitoring ice formation.[12] In particular, this work looks to progress from the previous study[13] through understanding the clear limitations of two-dimensional flow physics and noise and transcend into the higher-fidelity three-dimensional simulations to begin to accurately characterize the noise signals of rime and glaze ice structures. Neural networks based icing identification has been shown to be a powerful technique for in-flight ice detection.[14] Therefore, this work will train a neural network to map the acoustic noise signal produced from the ice structures to the performance indicators of the aircraft. It will thus help to restore parity in direct and indirect ice detection systems through occupying the void left by the rapid development of direct ice detection systems and the lack of development of indirect ice detection systems. The relationship between ice and noise is particularly interesting for rotorcraft as a severely iced rotor emits a significantly different broadband noise component to a clean rotor. In addition, one of the inherent adversities of rotorcraft is their symbolic noise generation and it is precisely this which this work seeks to exploit for a positive outcome in ice detection. What is more, the noise generation can be detected in real-time as well as in-flight as there is no lag between the generation of the ice and its respective noise counterpart.

In the present study, a new three-dimensional computational approach, which is capable of quantitatively characterizing rime and glaze ice types is introduced to continue to extend ice detection through computational aeroacoustics and Bayesian neural networks. In the text that follows, the methods behind the computations of the ice shapes, the high-fidelity simulation of the turbulent flow-field and acoustic propagation, and the machine learning using Bayesian neural networks are described in Section II. The results of the in-flight icing, the turbulent flow simulations and noise prediction of the different ice shapes, and design of a real-time in-flight ice detection system proceed in Section III. The concluding remarks of the papers are then drawn in Section IV.

II. Methodology

A. Ice Accretion

The in-house code PoliMIce is used for computing the ice accretion.[15] The PoliMIce software library provides state-of-the-art ice formation models. The model used in this work to capture the complex experimental ice shapes is the local exact solution of the unsteady Stefan problem for the temperature profiles within the ice layer in glaze conditions.[16] The ice shapes are then computed using a quasi-steady multi-step approach, whereby non-linear ice accretion is accounted for by iteratively updating the surface solution on which the ice accretes. At each multi-step iteration the collection efficiency is computed with a Lagrangian particle tracking code implementing trajectory and wall-impingement models to account for super-cooled large droplets as well as smaller particles.

B. Turbulent Flow Simulation and Noise Prediction using SU2

The SU2 open-source software suite was specifically developed for solving problems governed by partial differential equations (PDEs) and PDE-constraned optimization problems. It was developed with the aerodynamic shape optimization problems in mind. Therefore the suite is centered around a Reynolds-averaged Navier-Stokes (RANS) solver capable of simulating compressible, turbulent flows commonly found in problems in aerospace engineering. The governing equations are spatially discretized using the finite volume method, on unstructured meshes. A number of convective fluxes discretization schemes have been implemented, such as the Jameson-Schimdt-Turkel (JST) scheme and the upwind Roe scheme. The turbulence can be either modeled by the Spalart-Allmaras(S-A) model or the Menter Shear Stress Transport (SST) Model. For unsteady flows, a second-order dual time-stepping method can be used to obtain time-accurate solutions.

For scale-resolving capabilities, the Delayed Detached Eddy Simulation (DDES) based on the S-A model was implemented in SU2 by Molina[17] and has been demonstrated to successfully predict separated flows.[18,19] To overcome the slow transition from RANS to LES in shear-layer flows by reducing the so-called "grey area", a shear-layer adapted (SLA) sub-grid scale model[20] was implemented. In addition, to limit the numerical dissipation in LES part of the DDES model, the inviscid flux is computed using the so-called simple low dissipation advection upstream (SLAU2).[21]

For aeroacoustic prediction, a solid-surface Ffowcs Williams and Hawkings (FWH) analogy is used. To that end, Farassat's Formulation-1A (F1A)[22] has been implemented in the SU2 suite[23,24] which computes far-field noise from surface pressure fluctuations extracted from a preceding unsteady CFD simulation.

C. Machine Learning Using Bayesian Neural Networks

In this section, we briefly summarize NNs that does not capture uncertainty information, and BNNs that can provide uncertainty information to its predictions. Our goal is to build BNNs that map directly from acoustic signals to airfoil performance indicators.

A neural network (NN) maps input x to output $\hat{y}$: we write $\hat{y} = f(x)$ where the hat in $\hat{y}$ denotes NN *prediction*. For this paper we focus on densely connected feed-forward NNs for simplicity. For example, Fig. 1 shows a graphical representation of such a NN with an input layer, two hidden layers, and an output layer. The number of layers, number of nodes in each layer, and choice of ϕ_ℓ—together often referred to as hyperparameters—are usually selected before training, and choices leading to good performance are often unclear and require trial-and-error and experience. Nonetheless, once the network architecture is decided, the collection of all weights and all bias terms (which we denote by w) constitute the free parameters to be tuned. Accordingly, we update our notation to $\hat{y} = f(x;w)$.

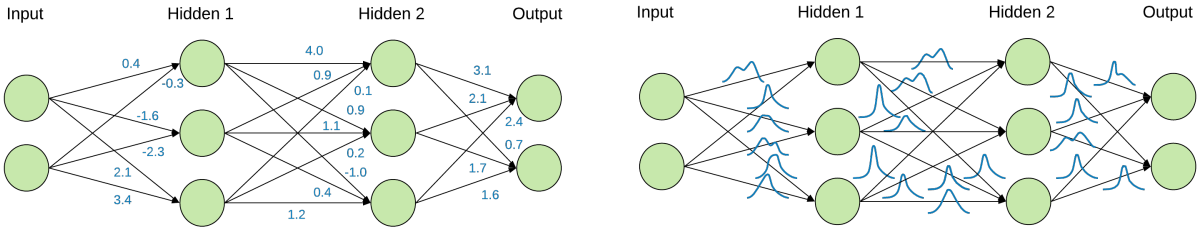

(a) Deep neural network

(b) Bayesian neural network

Figure 1: NN and BNN, each with an input layer, two hidden layers, and an output layer. Weights are shown in blue as deterministic values in NN, and as probability density functions in BNN.

Given N training data points in the form of input-output pairs $(x_T, y_T) = \{x_n, y_n\}_{n=1}^N$, DNN training typically involves choosing w to minimize a loss function that reflects the degree of mismatch between the DNN predictions and the true output values. For example, the least squares loss involves solving

$$w^* = \arg\min_w \left\{ \frac{1}{N} \sum_{n=1}^{N} [f(x_n;w) - y_n]^2 \right\}. \tag{1}$$

The optimization is often carried out with gradient-based algorithms, such as stochastic gradient descent.[25,26] However, regardless of how Eqn. (1) is solved, its solution returns a single-valued w^*. Consequently, the prediction at a

given input x is also single-valued: $\hat{y} = f(x; w^*)$, and it does not carry uncertainty information describing the quality and credibility of this predicted number.

BNNs treat w as random variables with associated probability density functions (PDFs) representing the uncertainty on w. When training data become available, these PDFs are updated through Bayes' theorem:

$$p(w|x_T, y_T) = \frac{p(y_T|x_T, w)p(w)}{p(y_T|x_T)}, \tag{2}$$

where $p(w)$ is the prior PDF on the weight parameters and we also assumed $p(w|x_T) = p(w)$ (i.e., the prior uncertainty should not change from knowing only the input values of the training data), $p(y_T|x_T, w)$ is the likelihood function, $p(w|x_T, y_T)$ is the posterior PDF, and $p(y_T|x_T)$ is the Bayesian evidence. Solving the Bayesian inference problem then entails computing the posterior $p(w|x_T, y_T)$—that is, our updated uncertainty on w given the training dataset (x_T, y_T).

Characterizing the full $p(w|x_T, y_T)$ is extremely challenging considering w can easily be thousands- or even millions-dimensional for DNNs arising from complex engineering and science applications. While Markov chain Monte Carlo-based algorithms[27] can generate samples from the true posterior PDF, the extreme dimensionality renders direct applications of these methods intractable. We thus seek to approximate the posterior through VI, thereby turning the sampling task into an optimization problem, which is generally computationally less intensive. The aim of VI is to approximate the posterior PDF with another PDF from a parametric (and usually standard-form) family that is "close" in some sense. Denoting the approximating family to be $q(w; \theta)$ parameterized by θ, the Kullback-Leibler (KL) divergence is often adopted to quantify the degree of dissimilarity between $q(w; \theta)$ and the true posterior $p(w|x_T, y_T)$:

$$D_{\mathrm{KL}}[q(w;\theta) \parallel p(w|x_T, y_T)] = \int_{-\infty}^{\infty} q(w;\theta) \log\left[\frac{q(w;\theta)}{p(w|x_T, y_T)}\right] dw = \mathbb{E}_{q(w;\theta)}\left[\log q(w;\theta) - \log p(w|x_T, y_T)\right]. \tag{3}$$

Solving the VI problem entails finding θ^* that yields the closest posterior approximation:

$$\theta^* = \arg\min_{\theta} D_{\mathrm{KL}}\left[q(w;\theta) \parallel p(w|x_T, y_T)\right]. \tag{4}$$

We note that while both are optimization statements, the objective function in Eqn. (4) is not directly comparable to the least squares loss in Eqn. (1) since they target different goals: Eqn. (1) aims to best fit the data, while Eqn. (4) seeks to best approximate the true posterior PDF that is defined through conditional probability.

In this paper, we explore Stein variational gradient descent (SVGD),[28] a non-parametric particle based method, to approach the VI problem above. This method leverages the relationship between the (functional) gradient of objective in Eqn. (4) to the Stein discrepancy, the latter which can be approximated using a set of particles. A gradient-descent procedure can then formed to iteratively minimize this gradient, as summarized by

$$w_i^{\ell+1} \leftarrow w_i^{\ell} + \varepsilon_\ell \hat{\phi}^*(w_i^{\ell}) \qquad \text{where} \qquad \hat{\phi}^*(w) = \frac{1}{m}\sum_{j=1}^{m}\left[k(w_j^{\ell}, w)\nabla_{w_j^{\ell}} \log p(w_j^{\ell}|x_T, y_T) + \nabla_{w_j^{\ell}} k(w_j^{\ell}, w)\right], \tag{5}$$

where $w_i^{\ell}, i = 1, \ldots, m$ represents the i-th particle at the ℓ-th iteration, ε_ℓ is the step size, $k(\cdot,\cdot)$ is a positive definite kernel. Furthermore, the gradient of the true log-posterior can be evaluated via the sum of gradients of log-likelihood and log-prior, since the gradient of the log-evidence is zero. The overall effect is an iterative transport of a set of points to match the target distribution $p(w|x_T, y_T)$. Figure 2 provides a visual illustration of the concept in a correlated bivariate Gaussian case. The advantage of SVGD is its ability to capture correlation as well as non-Gaussian structures. However, it may become computational expensive in high dimensions especially with a high number of particles.

III. Results

A. In-Flight Icing

The generation of complex ice shapes was achieved using the PoliMIce ice accretion software. To ensure the shape of the ice structures was representative of genuine in-flight icing scenarios, the computational ice shapes are validated against experimental icing results obtained from the NASA Glenn Icing Research Wind Tunnel (IRT). The computational results are assessed at various meteorological conditions to produce different severities of ice growth during both rime and glaze regimes. The test conditions used for the validation are based on the NASA Glenn IRT experimental work[29] and are shown in Table 1. The wind tunnel testing was performed on a untappered and untwisted NACA0012

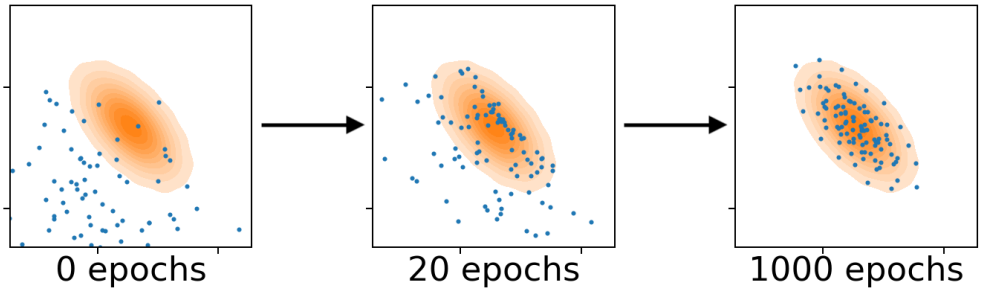

Figure 2: In this correlated bivariate Gaussian illustration, SVGD particles move to arrive at a better approximation to the posterior distribution.

wing with no sweep. Research from Zocca et al. has shown that the three-dimensional effects and the introduction of the wind tunnel walls in the NASA IRT has minimal influence on the ice shapes and so the ice accretion can be considered as two-dimensional.[30] The tests are grouped into low-temperature tests to produce rime ice structures and high-temperature tests to produce glaze ice structures. The overall time of exposure to icing lasted for 6 minutes to allow significant ice shapes to form. The supercooled water droplets Mean Volume Diameter (MVD) was held constant at $20\,g/m^3$. The tests were then divided into low-speed tests with high Liquid Water Content (LWC) and high-speed tests with low LWC. In total there is 8 experimental icing results – 4 rime and 4 glaze – used for the validation of the computational ice shapes.

Table 1: Meteorological conditions based on the experimental work at the NASA Glenn Icing Research Wind Tunnel.[29]

Run ID	Accretion Time $[s]$	Atmospheric Pressure $[Pa]$	Freestream Velocity $[m/s]$	Outside Air Temperature $[K]$	Liquid Water Content $[g/m^3]$	Mean Volume Diameter $[\mu m]$	Validation Data [-]
Rime 1	360	101325	67.05	247	1.00	20	Yes
Rime 2	360	101325	67.05	262	1.00	20	Yes
Rime 3	420	101325	102.82	247	0.55	20	Yes
Rime 4	420	101325	102.82	262	0.55	20	Yes
Glaze 1	360	101325	67.05	267.5	1.00	20	Yes
Glaze 2	360	101325	67.05	271	1.00	20	Yes
Glaze 3	420	101325	102.82	267.5	0.55	20	Yes
Glaze 4	420	101325	102.82	271	0.55	20	Yes

The resultant ice shapes are shown in Figure 3 and are compared against the NASA IRT test data.[29] The first group of simulations are the low-temperature tests which produce rime ice shapes and typically display spearhead like ice structures. The rime ice shapes are shown in Figures 3a, 3b, 3c and 3d and are in good agreement with the wind tunnel results. The thickness of ice is well represented as is the impingement limits of the ice. The second group of simulations are the high-temperature tests which produce glaze ice shapes and typically display double-horn ice structures. The glaze ice shapes are shown in Figures 3e, 3f, 3g and 3h and were found to be more difficult to replicate the wind tunnel results, however, remain in close proximity with the test data. The low-speed tests shown in Figures 3e and 3f reproduced the wind tunnel ice shapes markedly well, in particular the upper and lower horns. The high-speed tests shown in Figures 3g and 3h were found to be more challenging to simulate, although with the uncertainty within ice shapes being relatively high, minor discrepancies were inevitably expected.

The temperatures chosen were based on the experimental database.[29] The influence of the temperature on the ice shape is assessed and shown for the low-speed test conditions in Figure 4. It displays the transition from rime to glaze ice as the temperature is increased. During these conditions, it shows that temperatures below 262K are representative of rime ice. Temperatures ranging between 262-267.5K are indicative of mixed rime-glaze ice conditions. At the highest temperatures above 267.5K glaze ice becomes dominant.

With satisfactory validation of the ice shapes achieved, a test matrix to produce 50 samples for the machine learning

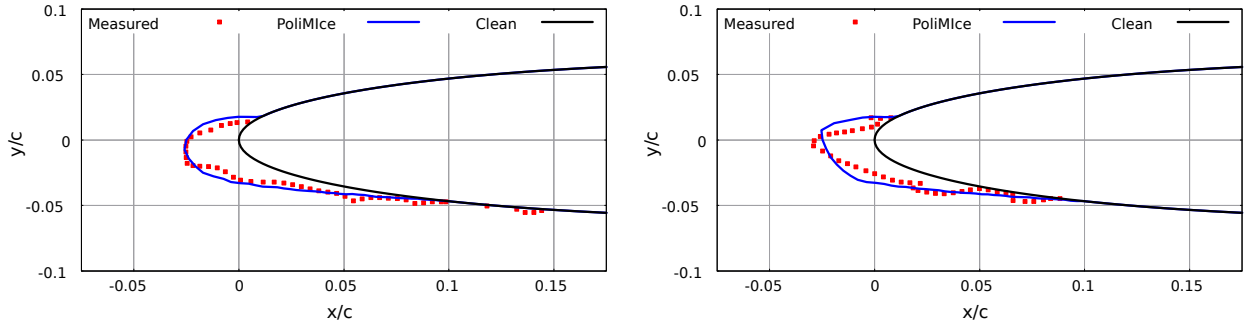

(a) Rime 1 ice shape.

(b) Rime 2 ice shape.

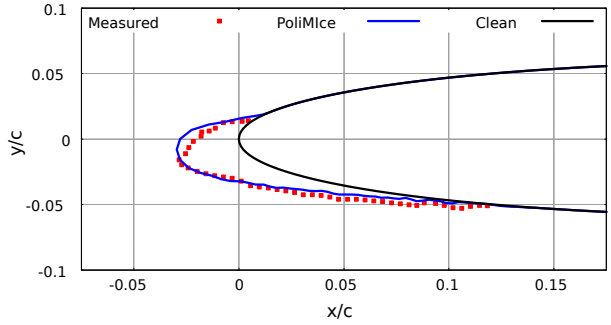

(c) Rime 3 ice shape.

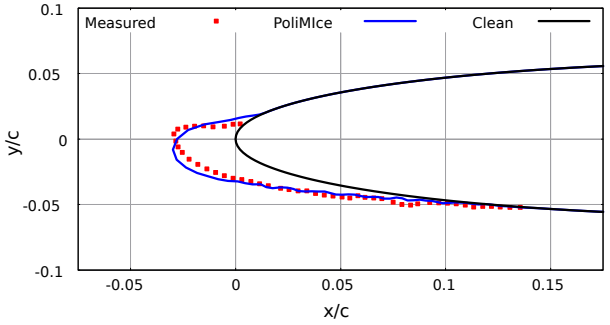

(d) Rime 4 ice shape.

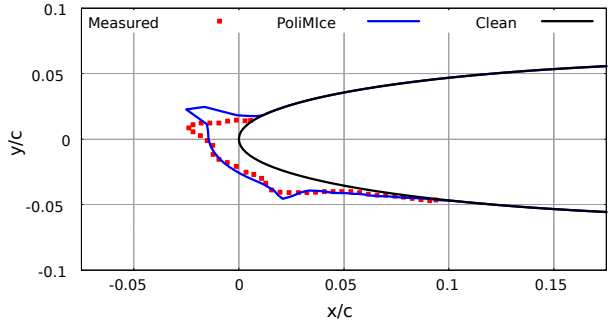

(e) Glaze 1 ice shape.

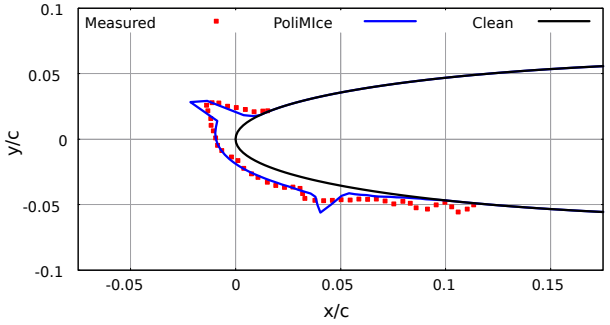

(f) Glaze 2 ice shape.

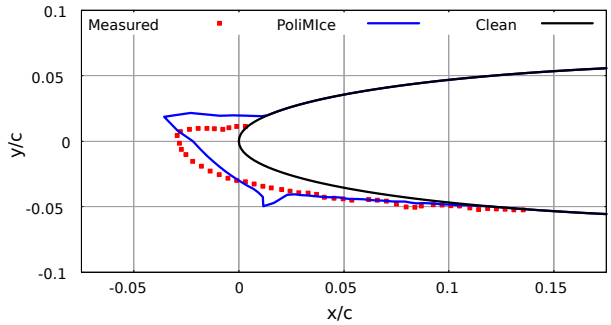

(g) Glaze 3 ice shape.

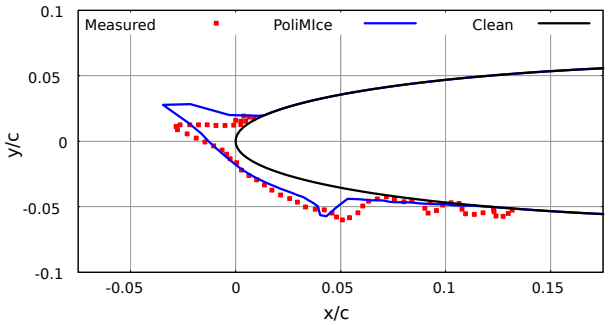

(h) Glaze 4 ice shape.

Figure 3: Validation of the computed ice shapes with the NASA IRT ice shapes in rime and glaze conditions.

was generated. The meteorological conditions were again modelled on the wind tunnel test data, except here the MVD of the particles was altered from $10 \rightarrow 120\,\mu m$. This allowed a range of ice shapes to be produced of varying severity. With the particle trajectories being computed using a Lagrangian based particle tracking code, simulations with supercooled larger water droplets (SLD) with an MVD of $120\,\mu m$ were also introduced into the sample set. Once

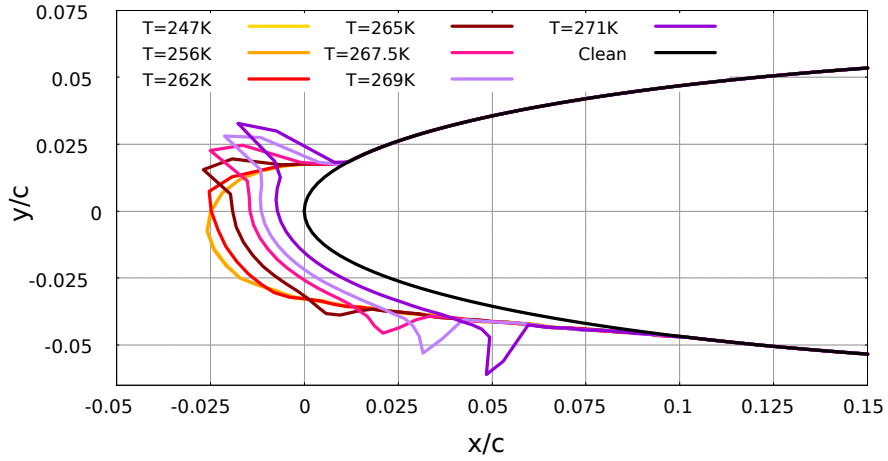

Figure 4: Influence of temperature on the ice shape displaying how the ice transitions from rime to glaze ice as the temperature increases.

again, the test conditions were grouped into conditions where rime ice and glaze ice would be produced.

Table 2: Test matrix to produce rime and glaze ice shapes.

Accretion Time $[s]$	Atmospheric Pressure $[Pa]$	Freestream Velocity $[m/s]$	Outside Air Temperature $[K]$	Liquid Water Content $[g/m^3]$	Mean Volume Diameter $[\mu m]$
			Rime		
360	101325	67.05, 102.82	247, 262	0.55, 1.00	10, 20, 30, 40, 50, 120
			Glaze		
360	101325	67.05, 102.82	267.5, 271	0.55, 1.00	10, 20, 30, 40, 50, 120

To incorporate important three-dimensional flow and noise features each of the ice shapes was then extruded by one chord length and a structured three-dimensional mesh was generated. With the ice shape only modelled as two-dimensional, this is a known limitation of the work, however, to produce true three-dimensional ice shapes would require significantly more costs with limited benefit. Three-dimensional ice shapes would also require very large mesh, and with the intention of using machine learning techniques, this was not deemed suitable. An exemplary the three-dimensional mesh of the two-dimensional extruded rime and glaze ice shapes is shown in Figure 5. The spanwise extent used in this work is $S = 1.0C$, discretized with 33 points. The mesh with a wing exposed to rime ice is shown in Figure 5a and was generated using 4 blocks and contains a total of just over 700, 000 elements. The mesh with a wing exposed to glaze ice is shown in Figure 5b and was generated using 6 blocks and contains a total of just over 800, 000 elements.

B. Turbulent Flow Simulation and Noise Prediction for Different Ice Shapes

To compare the turbulent flow field and far-field noise features of the clean and iced airfoils, the clean NACA0012 airfoil as well as a rime and a glaze ice airfoil (Rime 4 and Glaze 4 on Table 1) are simulated with meshes of 8 million elements using the DDES-FWH approach outlined in Section II. B. The airfoil section is set to pitch around a spanwise axis passing through its quarter-chord point. Sinusoidal pitching motion is prescribed with a mean angle of attack (AoA) of 6°, pitching amplitude of 6°, and pitching frequency of 17.0 Hz. A time step of $\Delta t = 0.01C/U_\infty = 0.0001s$ is used, which results in 600 time-steps within each pitching cycle. The flow statistics and acoustics are computed after the 8th pitching cycle, over 20 pitching cycles. The instantaneous flow fields at AoA=3° on the upstroke are visualized by the iso-surfaces of the Q-criterion colored by vorticity magnitude, as shown on Figure 6. The effect of leading-edge icing is evident. The clean airfoil shows quasi-2D flow structures as flow remains mostly attached over the suction side. Detached eddies signifying separated flow can clearly be seen in the rime ice airfoil shows whereas the more

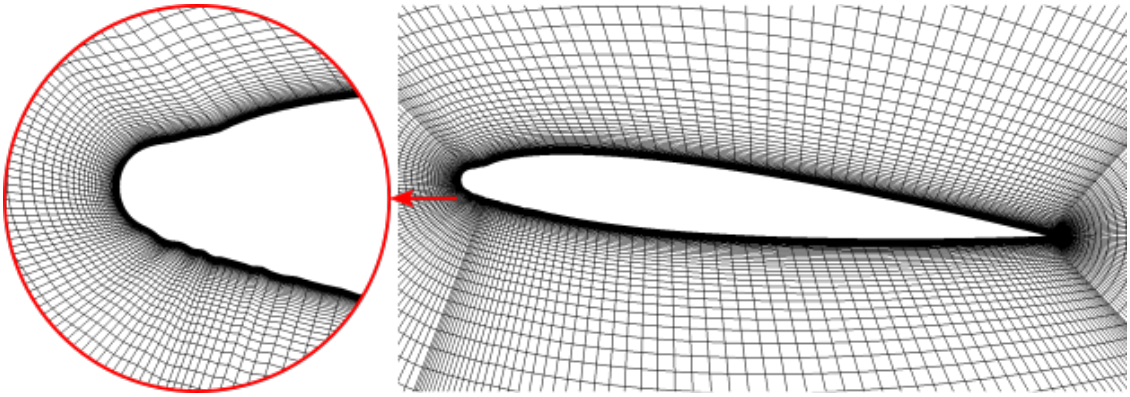

(a) An exemplary sectional cut-out of a structured rime mesh displaying an enlarged view of the leading-edge.

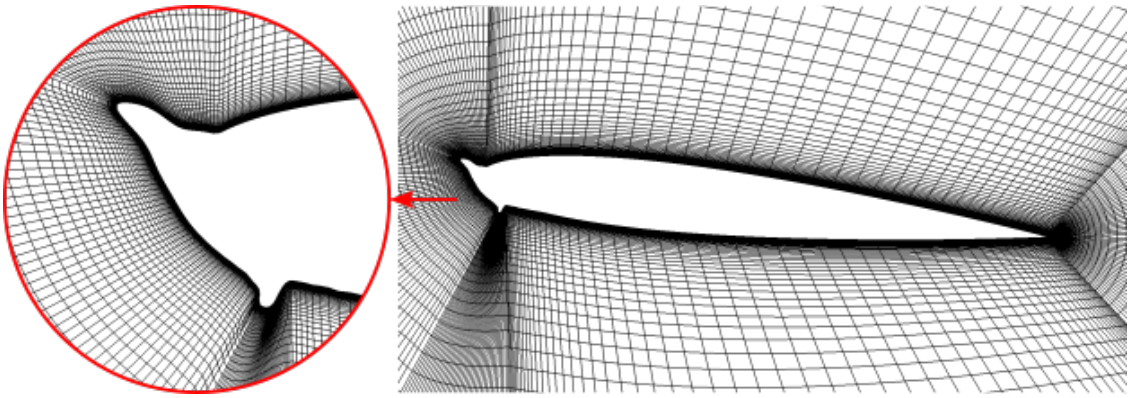

(b) An exemplary sectional cut-out of a structured glaze mesh displaying an enlarged view of the leading-edge.

Figure 5: Quasi-2D iced mesh achieved through extruding the validated 2D ice shapes.

severely iced (glaze ice) airfoil shows more fine-scale, three-dimensional turbulent structures over the entire suction side. Note that even though the ice shapes are quasi-2D, the resolved turbulent structures by DDES are very much three-dimensional, especially in the glaze ice case where the Kelvin-Helmholtz instability is triggered immediately past the ice horn and develops quickly into 3D turbulence. This is in stark contrast to the result of the unsteady RANS simulation, computed on the same glaze ice airfoil with the same mesh as shown on Figure 10a – only two-dimensional structures that are unphysically spanwisely coherent can be seen. The time histories of the lift and drag coefficients of the rime and glaze ice airfoils, computed using RANS and DDES simulations are compared on Figure 7. In the case of mild, rime-type ice, the force coefficients predicted by URANS and DDES are very similar. Noticeable differences exist in the glaze ice case where URANS under-predicts the maximum lift coefficient by around 20%. This is because the lack of resolved turbulence in URANS causes the flow to prematurely separate immediately behind the horn over the entire suction side, as can be seen by comparing the wall shear stress of the glaze ice airfoil at that time instance between URANS (Figure 10b) and DDES (Figure 8c) predictions. Both clean and rime ice airfoils show trailing edge separation on Figure 8 due to the dynamic effect of the upstroke. Surface noise footprints visualized by the instantaneous wall pressure fluctuation of the clean, rime and glaze ice airfoil sections are compared in Figure 9. The clean and rime ice airfoils exhibit similar surface noise footprints. On the other hand, the glaze airfoil exhibits a highly irregular noise footprint pattern with significant spatial frequency content. One may already speculate that the far-field noise signature of the glaze ice should be associated with elevated high-frequency contents. This is confirmed by the far-field noise spectra shown on Figure 11 – while the rime ice airfoil shows a slight increase of high-frequency noise over the clean airfoil, the glaze airfoil has a significantly elevated noise level over the entire high-frequency range up to the cutoff. It is worth noting that the wall pressure fluctuation predicted by URANS at the same time instance for the glaze airfoil appears to be quasi-2D (Figure 10c), lacking any spanwise variation, consistent with the observation on its Q-criterion iso-surface (Figure 10a).

The results above highlight two important points:

1. To accurately predict the three-dimensional turbulent flow field and noise source of iced airfoil sections, espe-

cially in the case of severe glaze ice shapes, scale-resolving simulations such as DDES is necessary. Unsteady RANS simulations are inadequate as they are unable to predict the separated turbulent flow behind the leading edge ice structure.

2. The more severe the leading edge ice accretion is, the more elevated the high-frequency range of the far-field noise tends to be. This can be exploited as a distinguishing feature in a machine learning model to build a mapping between the far-field noise level and ice shape as well as the associated aerodynamic performance of the ice airfoil.

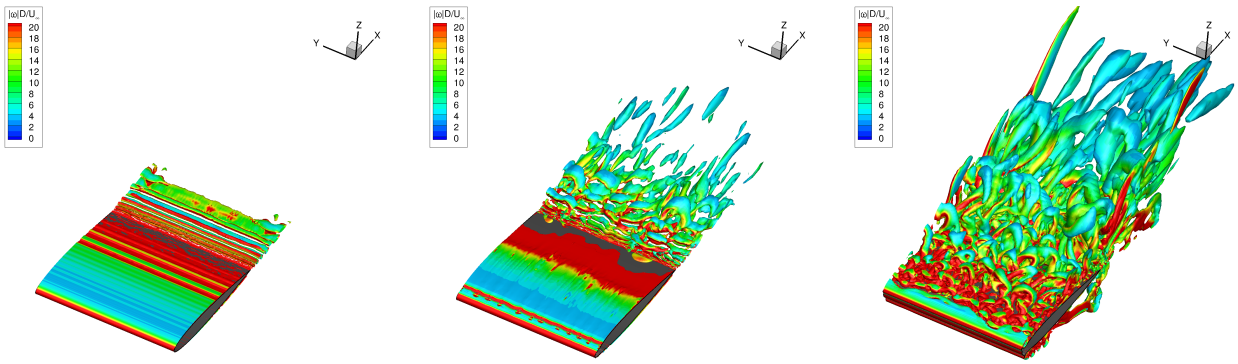

(a) Clean NACA0012 (b) Rime ice (c) Glaze ice

Figure 6: Instantaneous vortical structures of the clean NACA0012, rime and glaze ice airfoil sections at AoA=3° on blade upstroke, visualized by iso-surfaces of the Q-criterion colored by vorticity magnitude

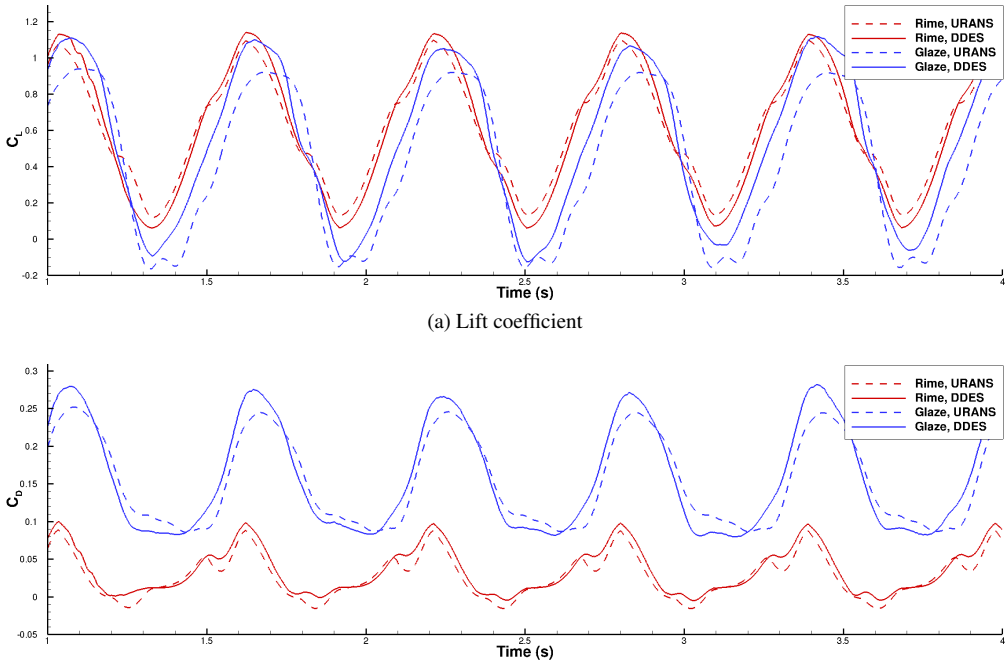

(a) Lift coefficient

(b) Drag coefficient

Figure 7: Time histories of lift and drag coefficients of the rime and glaze ice airfoils computed using unsteady RANS and DDES simulations

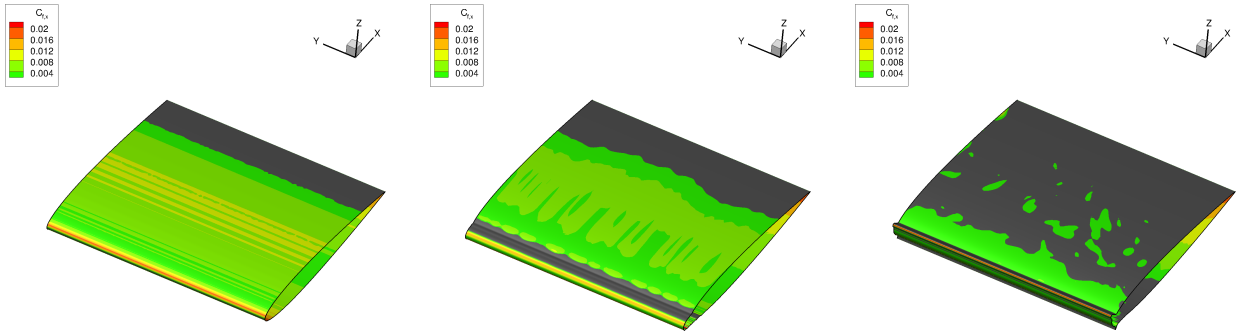

(a) Clean NACA0012 (b) Rime ice (c) Glaze ice

Figure 8: Instantaneous wall shear stress at AoA=3° on blade upstroke, showing the extent of flow separation (grey area) of the clean NACA0012, rime and glaze ice airfoil sections

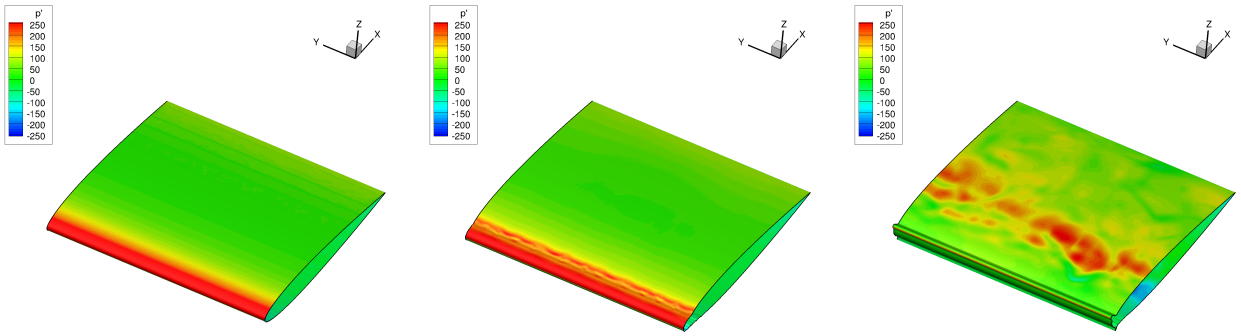

(a) Clean NACA0012 (b) Rime ice (c) Glaze ice

Figure 9: Surface noise footprint visualized by the instantaneous wall pressure fluctuation of the clean NACA0012, rime and glaze ice airfoil sections at AoA=3° on blade upstroke

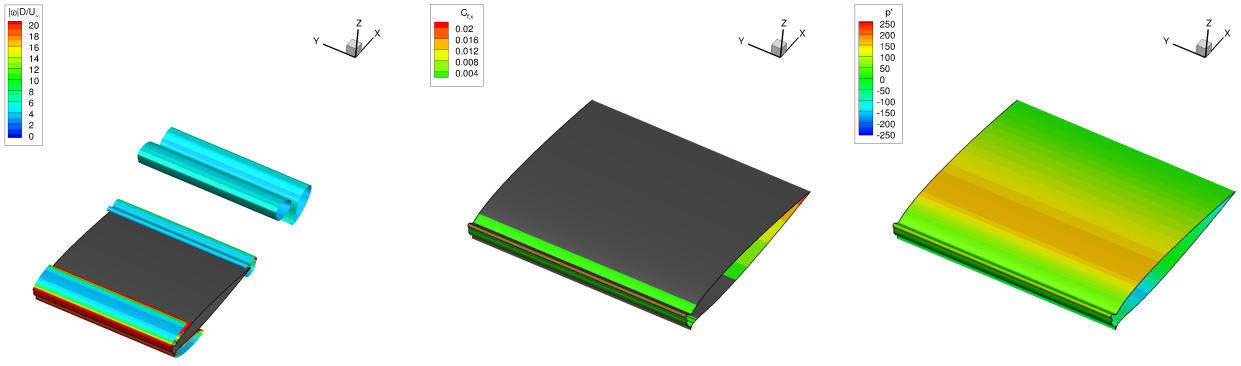

(a) Q-criterion colored by vorticity magnitude (b) Wall shear stress (separated region in grey) (c) Wall pressure fluctuation

Figure 10: Instantaneous Q-criterion, wall shear stress and wall pressure fluctuation of the glaze airfoil section at AoA=3° on blade upstroke, computed by an unsteady RANS simulation

C. Preliminary Design of A Real-Time In-Flight Ice Detection System

A total of 40 rime ice and 40 glaze ice shapes are generated using the DDES-FWH approach outlined in Section II. In preparation of building the BNNs, training data are pre-processed by computing the log values of power spectral

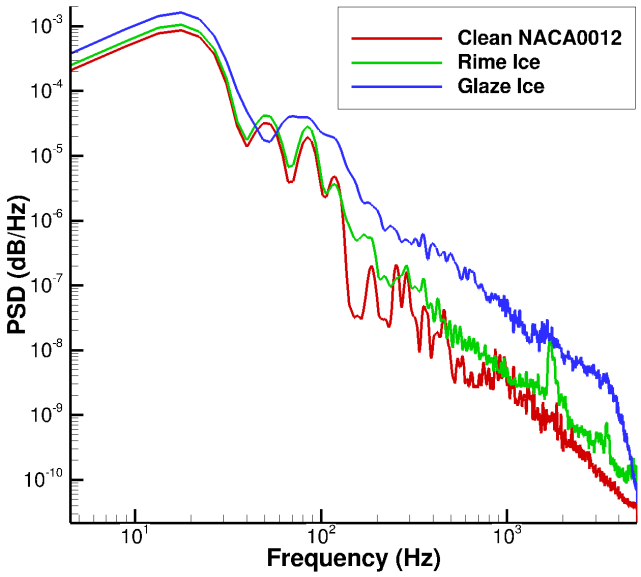

Figure 11: Far-field sound spetra of the clean NACA0012, rime and glaze ice airfoil sections, computed 20C below the center of rotation of the pitching airfoil

density (PSD) for each data signal, then discretizing into 119 bins covering the frequency range 17–1000 Hz, and lastly shifting and standardizing all values using the mean and standard deviation statistics from across all training data simulations. From each simulation, we extract from its hysteresis loop the minimum, maximum, and mean values of C_L and C_M—these 6 quantities are designated as the output QoIs for our BNNs. The prior $p(w)$ in Eqn. (2) is chosen to be independent Gaussian $w_k \sim \mathcal{N}(0, 10^2)$, and the likelihood $p(y_T|x_T, w)$ is constructed to reflect an additive independent Gaussian data noise $y_k = f(x_k; w) + \varepsilon_k, \varepsilon_k \sim \mathcal{N}(0, 0.1^2)$. Table 3 summarizes the BNN architecture adopted in our investigation, leading to a total of $K = 8,856$ network weights modeled by 50 Stein variational particles. We use 41 cases for training, and reserve the rest for testing.

Table 3: BNN architecture

Layer	Name	No. of Neurons	Activation Fcn.
1	input	119	-
2	hidden 1	50	tanh
3	hidden 2	50	tanh
4	output	6	linear

Figure 12 presents the BNN predictions at 10 test data points for the rime and glaze ice types, using the same single BNN trained from the 60 points. Uncertainty information is now available for each QoI prediction, reflecting uncertainty induced by the quantity and quality of training data. Both rime and glaze ice have similar levels of accuracy, while glaze ice has clearly larger uncertainty. In addition, we see that rime cases appear to collect around three clusters of possible C values while glaze cases tend to cover a wider range in comparison. This suggests the possibility that additional rime simulations are already reasonably covered by (or similar to) current data points from these clusters whereas new glaze simulations may be quite different from its existing cohorts, and so the glaze response might be more difficult to capture by the BNN as a result and as seen by the slightly more off-diagonal values in the right sub-figure. However, we caveat that there are additional factors affecting the overall performance of BNN under each ice type, such as the nonlinearity of the true underlying response and the sensitivity and informative of each available training case. Furthermore, we note that an "accurate" BNN does not necessarily imply lower uncertainty, since the uncertainty in the model is completely defined through Bayes' Theorem and conditioned on the training data

at hand. The degree of uncertainty also varies among different test points (i.e., under different ice profiles) and for different QoIs. Figure 13 provides an example of the full posterior predictive densities for different pairs of the 6 QoIs at a specific test point (case 'Glaze 10'). The densities appear unimodal and exhibiting some non-Gaussian structure. Evaluation of this predictive uncertainty using a 50-particle setting takes about 0.8 ms on a 6 core 2.6 GHz Intel i7 processor, and is promising for real-time requirements. Overall, this information can be extremely useful for pilot decision-making in assessing the icing condition as well as the extent of relying the decision on the ML prediction. Furthermore, it can also be used to identify challenging ice profiles for targeting additional training simulations, and performing optimal experimental design. Going forward, we seek to acquire additional training data to further improve the BNN performance, and also to incorporate other sources of uncertainty such as the noise signal measurement error and model-form error from the selected NN architecture.

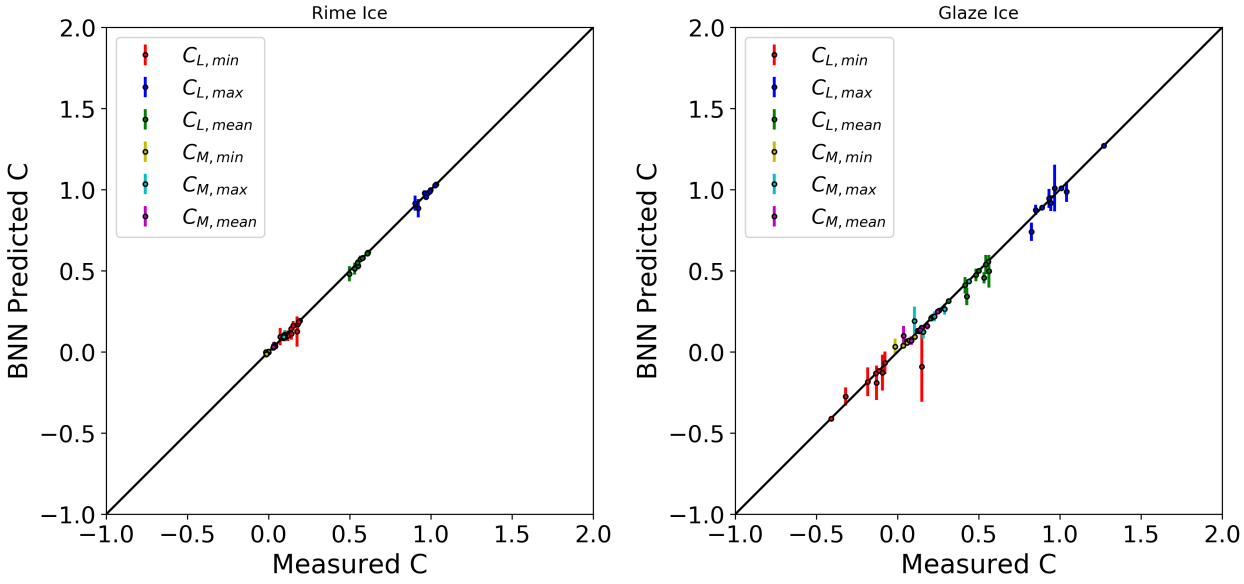

Figure 12: Predictions of 10 rime (left) and 10 glaze (right) ice cases showing posterior-predictive distribution mean and ± 1.96 standard deviations.

IV. Conclusion

In this work, we propose a novel approach towards developing a real-time in-flight ice detection system using computational aeroacoustics and Bayesian neural networks. In particular, a high-fidelity DDES-FWH solver in SU2 is used to compute both the aerodynamic forces of airfoil sections with various levels of ice accretion, as well as their corresponding far-field noise levels. The dataset generated is then used to construct a Bayesian neural network that provides (1) mapping from observed far-field broadband noise level to predictions of aerodynamic performance indicators, and (2) uncertainty information indicating the quality and credibility of these predictions. While the icing simulation, aeroacoustic prediction as well as the construction of Bayesian neural network model all require potentially extensive computational resources in the *offline* phase, the prediction of aerodynamic performance indicators based on measured far-field noise level as well as their associated uncertainty information can both be obtained rapidly in the time-critical *online* phase in-flight.

To the best of our knowledge, this work is the first to employ high-fidelity aeroacoustic simulations to develop correlations between aerodynamic performance and far-field noise level of iced airfoil sections via machine learning techniques. That being said, it should also be noted that the current work as-is only serves as a proof-of-concept study. It is clear that the quasi-2D pitching airfoil considered in this study is a highly simplified representation of the complex rotorcraft icing problem in real life which involves turbulent blade-vortex interaction with rotating blades and three-dimensional ice formation along the blades. Various noise sources such as those from multiple rotors and engines, as well as rotor-fuselage interaction must be taken into account and differentiated in developing an ice detection system using the multi-disciplinary framework proposed in the current work.

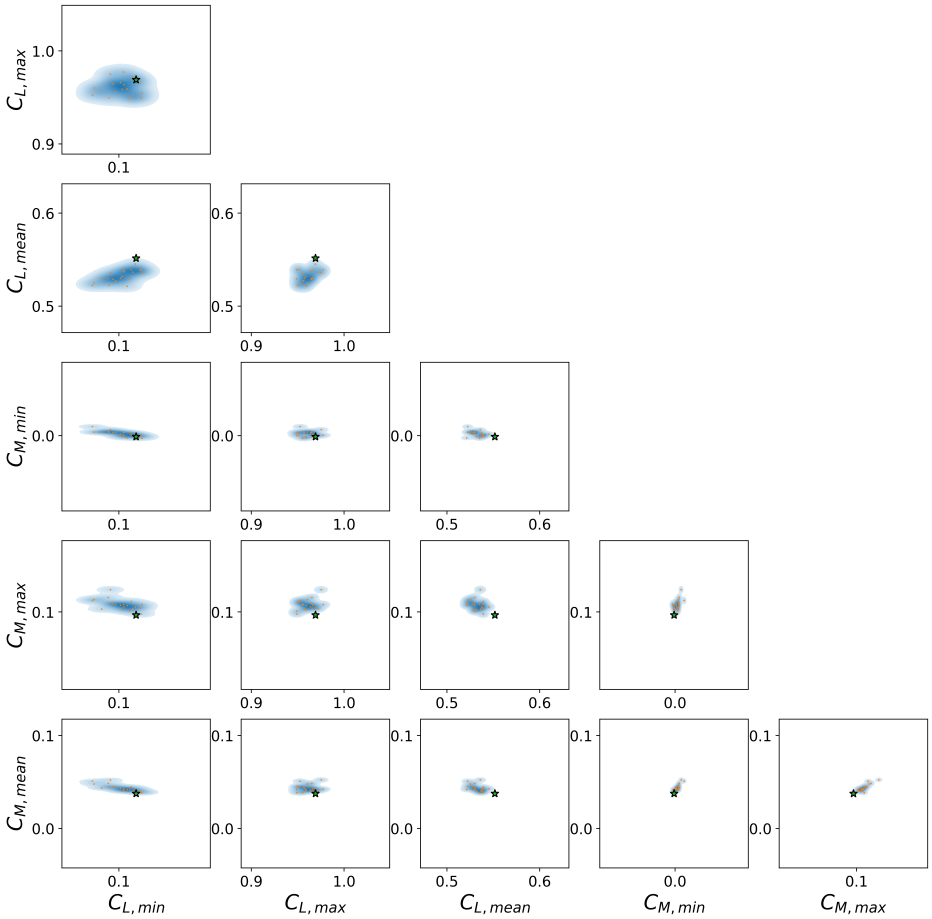

Figure 13: Posterior predictions of Run ID 'Glaze 10', one of the 10 test points not part of the training set. The star symbol indicates the true value of quantities being predicted. The orange dots are the SVGD particles and the blue density plot is a kernel density estimate from these particles.

V. Acknowledgement

The computational resources provided by the RHRK high performance computing center via the 'Elwetritsch' high performance cluster at the TU Kaiserslautern is gratefully acknowledged. The work from Politecnico di Milano has received funding from the European Union's H2020 research and innovation programme under the Marie Skłodowska-Curie grant agreement No 721920. Further information can be found at the Network for Innovative Training on ROtorcraft Safety (NITROS) project website.

References

[1]Gent, R., Dart, N., and Cansdale, J., "Aircraft icing," *Philosophical Transactions of the Royal Society of London. Series A: Mathematical, Physical and Engineering Sciences*, Vol. 358, No. 1776, 2000, pp. 2873–2911.

[2]Roach, W., Forrester, D. A., Crewe, M. E., and Watt, K. F., "An icing climatology for helicopters," *Royal Meteorological Office Special Investigations Memo*, , No. 9, April 1984, pp. 41.

[3]NTSB, "National Transportation Safety Board Aviation Accident Final Report," NTSB No. WPR17FA047, December 2017.

[4]NTSB, "National Transportation Safety Board Aviation Accident Final Report," NTSB No. WPR16LA104, June 2018.

[5]NTSB, "National Transportation Safety Board Aviation Accident Final Report," NTSB No. ANC16FA023, January 2018.

[6]Thomas, S. K., Cassoni, R. P., and MacArthur, C. D., "Aircraft anti-icing and de-icing techniques and modeling," *Journal of Aircraft*, Vol. 33, No. 5, 1996, pp. 841–854.

[7]C. Pellissier, M., Habashi, W., and Pueyo, A., "Optimization via FENSAP-ICE of aircraft hot-air anti-icing systems," *Journal of Aircraft*, Vol. 48, No. 1, 2011, pp. 265–276.

[8]Pourbagian, M. and Habashi, W. G., "Surrogate-based optimization of electrothermal wing anti-icing systems," *Journal of Aircraft*, Vol. 50, No. 5, 2013, pp. 1555–1563.

[9]DiPlacido, N., Soltis, J., and Palacios, J., "Enhancement of ultrasonic de-icing via tone burst excitation," *Journal of Aircraft*, Vol. 53, No. 6, 2016, pp. 1821–1829.

[10]Bragg, M., Gregorek, G., and Lee, J., "Airfoil aerodynamics in icing conditions," *Journal of aircraft*, Vol. 23, No. 1, 1986, pp. 76–81.

[11]Zhao, X. and Rose, J. L., "Ultrasonic guided wave tomography for ice detection," *Ultrasonics*, Vol. 67, 2016, pp. 212–219.

[12]Cheng, B., Han, Y., Brentner, K. S., Palacios, J., Morris, P. J., Hanson, D., and Kinzel, M., "Surface roughness effect on rotor broadband noise," *International Journal of Aeroacoustics*, Vol. 17, No. 4-5, 2018, pp. 438–466.

[13]Zhou, B. Y., Gauger, N. R., Hauth, J., Huan, X., Morelli, M., and Guardone, A., "Towards Real-Time In-Flight Ice Detection Systems via Computational Aeroacoustics and Machine Learning," *AIAA Aviation 2019 Forum*, 2019, p. 3103.

[14]Caliskan, F. and Hajiyev, C., "A review of in-flight detection and identification of aircraft icing and reconfigurable control," *Progress in Aerospace Sciences*, Vol. 60, 2013, pp. 12–34.

[15]Gori, G., Zocca, M., Garabelli, M., Guardone, A., and Quaranta, G., "PoliMIce: A simulation framework for three-dimensional ice accretion," *Applied Mathematics and Computation*, Vol. 267, September 2015, pp. 96–107.

[16]Gori, G., Parma, G., Zocca, M., and Guardone, A., "Local Solution to the Unsteady Stefan Problem for In-Flight Ice Accretion Modeling," *Journal of Aircraft*, Vol. 55, No. 1, 2017, pp. 251–262.

[17]Molina, E., *Detached Eddy Simulation in SU2*, Ph.d. thesis, Aeronautical Institute of Technology, 2015.

[18]Molina, E. M., Zhou, B. Y., Alonso, J. J., Righi, M., and da Silva, R. G., "Flow and Noise Predictions Around Tandem Cylinders using DDES approach with SU2," AIAA-2019-0326, 2019.

[19]Molina, E. S., Silva, D. M., Broeren, A. P., Righi, M., and Alonso, J. J., "Application of DDES to Iced Airfoil in Stanford University Unstructured (SU2)," *Progress in Hybrid RANS-LES Modelling*, edited by Y. Hoarau, S.-H. Peng, D. Schwamborn, A. Revell, and C. Mockett, Springer International Publishing, Cham, 2020, pp. 283–293.

[20]Shur, M. L., Spalart, P. R., Strelets, M. K., and Travin, A. K., "An Enhanced Version of DES with Rapid Transition from RANS to LES in Separated Flows," *Flow, Turbulence and Combustion*, Vol. 95, No. 4, 2015, pp. 709–737.

[21]Kitamura, K. and Hashimoto, A., "Reduced Dissipation AUSM-family Fluxes: HR-SLAU2 and HR-AUSM+-up for High Resolution Unsteady Flow Simulations," *Computers & Fluids*, Vol. 126, 2016, pp. 41–57.

[22]Farassat, F., "Derivation of Formulations 1 and 1A of Farassat," *NASA/TM-2007-214853. NASA Langley Research Center*, 2007.

[23]Zhou, B. Y., Albring, T., Gauger, N. R., Ilario, C. R., Economon, T. D., and Alonso, J. J., "Reduction of Airframe Noise Components Using a Discrete Adjoint Approach," AIAA-2017-3658, 2017.

[24]Icke, R. O., Baysal, O., Moy, A., Lopes, L., Zhou, B. Y., and Diskin, B., "Toward Adjoint-Based Aeroacoustic Optimization for Propeller and Rotorcraft Applications," *Submitted to AVIATION 2020 Forum*, 2020.

[25]LeCun, Y. A., Bottou, L., Orr, G. B., and Müller, K.-R., "Efficient BackProp," *Neural Networks: Tricks of the Trade*, edited by G. Montavon, G. B. Orr, and K.-R. Müller, Springer-Verlag Berlin Heidelberg, 2012, pp. 9–48.

[26]Robbins, H. and Monro, S., "A Stochastic Approximation Method," *The Annals of Mathematical Statistics*, Vol. 22, No. 3, 1951, pp. 400–407.

[27]Gilks, W. R., Richardson, S., and Spiegelhalter, D. J., *Markov Chain Monte Carlo in Practice*, Chapman & Hall, New York, NY, 1996.

[28]Liu, Q. and Wang, D., "Stein Variational Gradient Descent: A General Purpose Bayesian Inference Algorithm," *Advances in Neural Information Processing Systems 29 (NIPS 2016)*, Barcelona, Spain, 2016, pp. 2378–2386.

[29]Shin, J. and Bond, T. H., "Experimental and computational ice shapes and resulting drag increase for a NACA 0012 airfoil," NASA Technical Memorandum No. 105743, January 1992.

[30]Zocca, M., Gori, G., and Guardone, A., "Wind Tunnel Blockage and Three-dimensional Effects in Wind Tunnel Testing of Ice Accretion Over Airfoils and Wings," *Main Thematic Areas*, 2014, pp. 233.